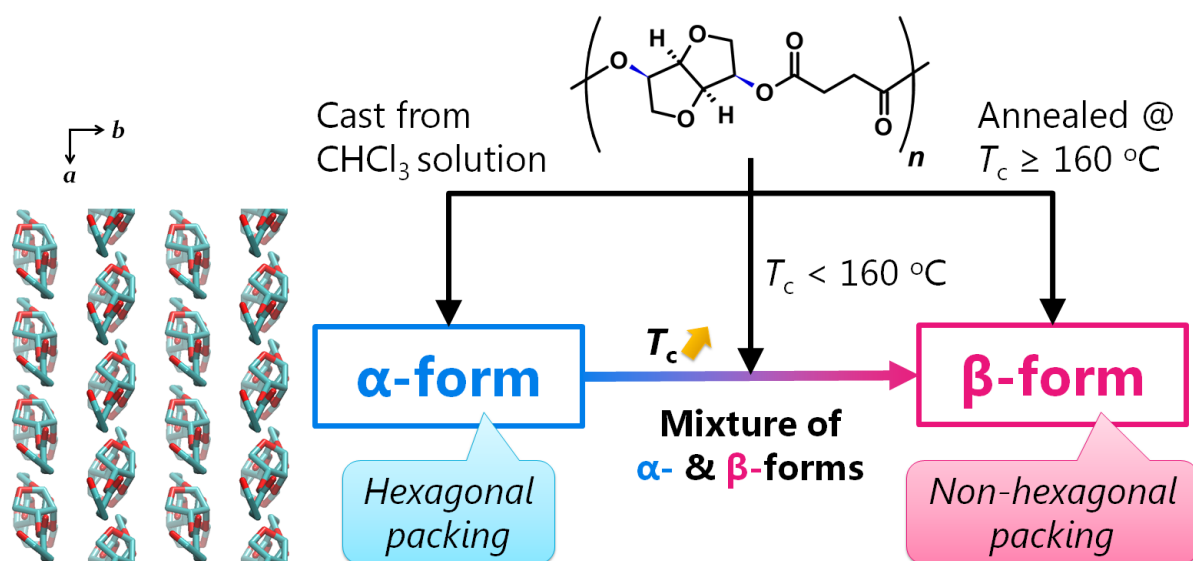


## Supporting Information

**Crystal Polymorphism of Biobased Polyester Composed of Isomannide and Succinic Acid**Hironori MARUBAYASHI,<sup>\*,†,‡</sup> Takaaki USHIO,<sup>†</sup> & Shuichi NOJIMA<sup>†,‡</sup><sup>†</sup> Department of Chemical Science and Engineering, School of Materials and Chemical Technology, &<sup>‡</sup> Research Institute of Polymer Science and Technology (RIPST), Tokyo Institute of Technology,

2-12-1 Ookayama, Meguro-ku, Tokyo 152-8552, Japan



## S1. 1,4:3,6-Dianhydrohexitols (Isohexides)

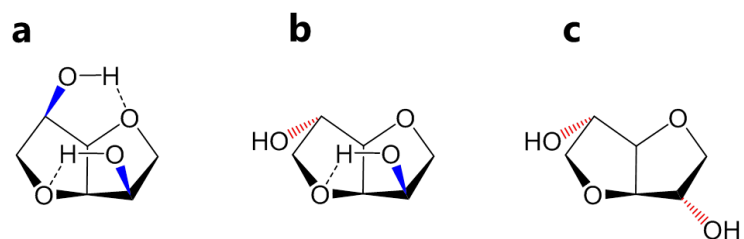
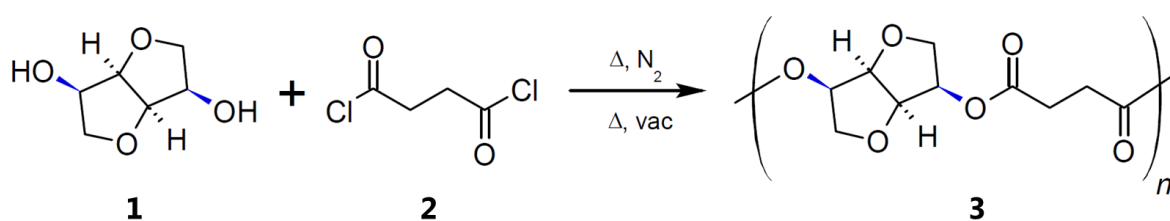


**Fig. S1.** Chemical structures of 1,4:3,6-dianhydrohexitols (isohexides): (a) isomannide, (b) isosorbide, and (c) isoidide. Dotted lines (a, b) represent intramolecular hydrogen bonds.

## S2. Polymerization of M4



**Scheme S1.** Synthesis of polyester (M4, **3**) from isomannide (**1**) and succinyl chloride (**2**).

### S3. Intensity Correction for 1D WAXD Data

Intensity of circularly-averaged 1D profiles ( $I_{\text{obs}}$ ) was corrected to  $I_{\text{cor}}$  by considering contributions of absorption ( $A$ ), polarization ( $P$ ), air-absorption ( $A_{\text{air}}$ , so-called "inverse square law"), and air-scattering factors ( $I_{\text{air}}$ ), according to the following equation.

$$I_{\text{obs}} = A \cdot P \cdot A_{\text{air}} \cdot I_{\text{cor}} + I_{\text{air}} \quad (\text{S1})$$

### S4. Crystallinity Determination by 1D WAXD

The degree of crystallinity ( $X_c$ ) was evaluated from WAXD curves [ $I(2\theta)$  vs  $2\theta$ , where  $I(2\theta)$  is the diffraction intensity and  $\theta$  is the Bragg angle] according to the following equation:

$$X_c = \frac{\int_{2\theta_1}^{2\theta_2} I_c(2\theta) d(2\theta)}{\int_{2\theta_1}^{2\theta_2} I(2\theta) d(2\theta)} \times 100 \quad (\text{S2})$$

where  $2\theta_1$  is  $8^\circ$ ,  $2\theta_2$  is  $40^\circ$ ,  $I_c(2\theta)$  is the diffraction intensity from the crystalline phase, and  $I(2\theta)$  is the intensity from both the crystalline and amorphous phases [ $I_c(2\theta) + I_a(2\theta)$ ].  $I_c(2\theta)$  was evaluated by using the melt-quenched [ $I_c(2\theta) = 0$ ] and melt-crystallized [ $I_c(2\theta) > 0$ ] samples. Representative WAXD curves of M4 samples with the fitted amorphous curve [ $I_c(2\theta) = 0$ ] are shown in Fig. S2.

### S5. Intensity Correction for 2D WAXD Data (Fiber Diagram)

Intensity of fiber diagrams ( $I_{\text{obs}}$ ) was corrected to  $I_{\text{cor}}$  by considering contributions of absorption ( $A$ ), polarization ( $P$ ), Lorentz ( $L$ ), air-absorption ( $A_{\text{air}}$ , so-called "inverse square law"), and air-scattering factors ( $I_{\text{air}}$ ), according to the following equation.

$$I_{\text{obs}} = A \cdot P \cdot L \cdot A_{\text{air}} \cdot I_{\text{cor}} + I_{\text{air}} \quad (\text{S3})$$

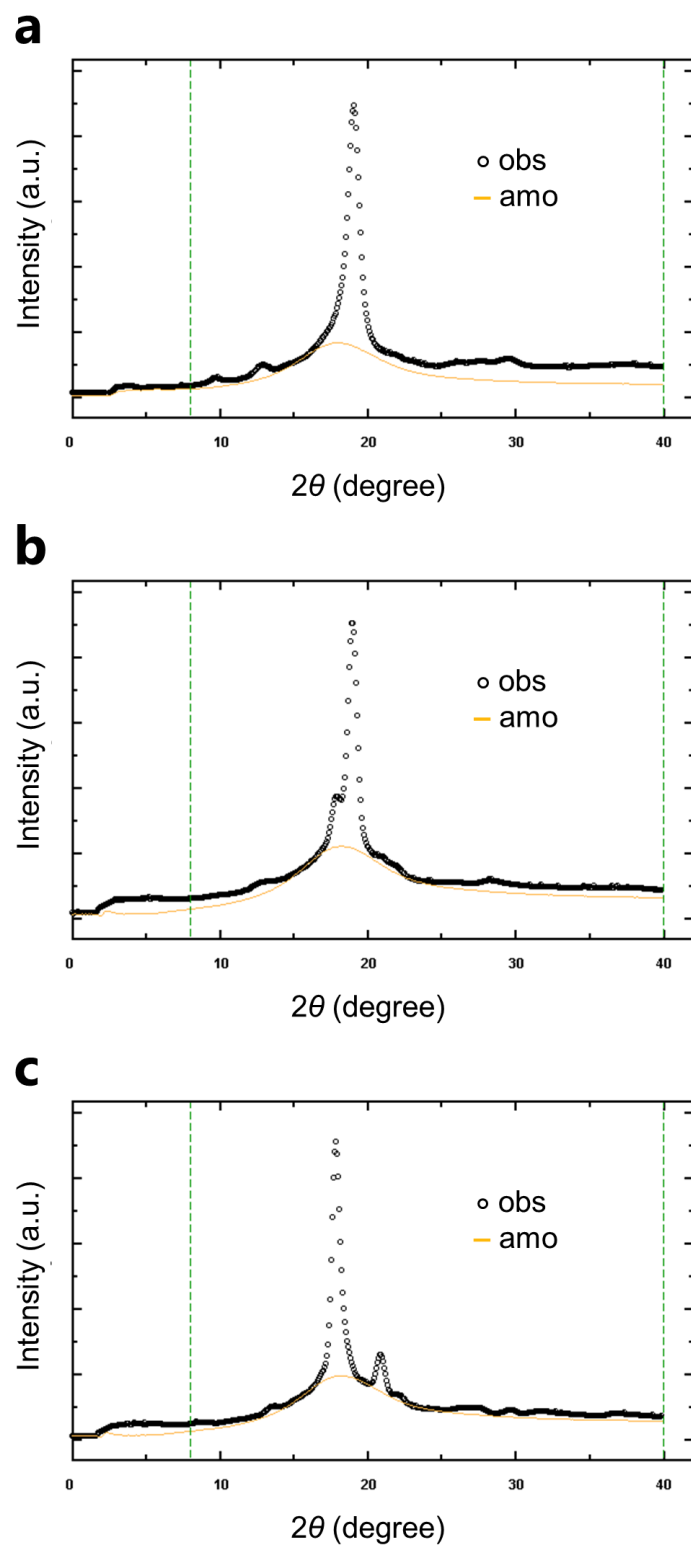


**Fig. S2.** WAXD curves of M4 crystallized in various conditions. (a) The  $\alpha$ -form sample obtained by solution casting (chloroform), (b) the  $\alpha$ -form-rich sample by melt-crystallization at 120 °C, and (c) the  $\beta$ -form sample by melt-crystallization at 170 °C. Fitted amorphous curve (yellow) is shown for each sample.  $X_c$  is calculated at  $2\theta = 8\text{--}40^\circ$ , as shown by green dotted lines.

## S6. Effect of Casting Solvent Species on Crystal Structure

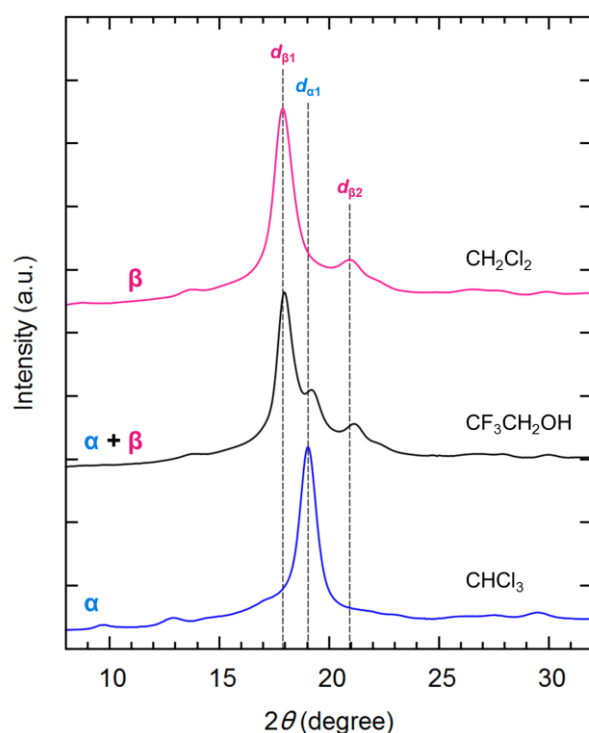


**Fig. S3.** WAXD curves of M4 crystallized by various casting solvents at room temperature.

## S7. Effect of Re-annealing on Crystal Structure of Cast Sample

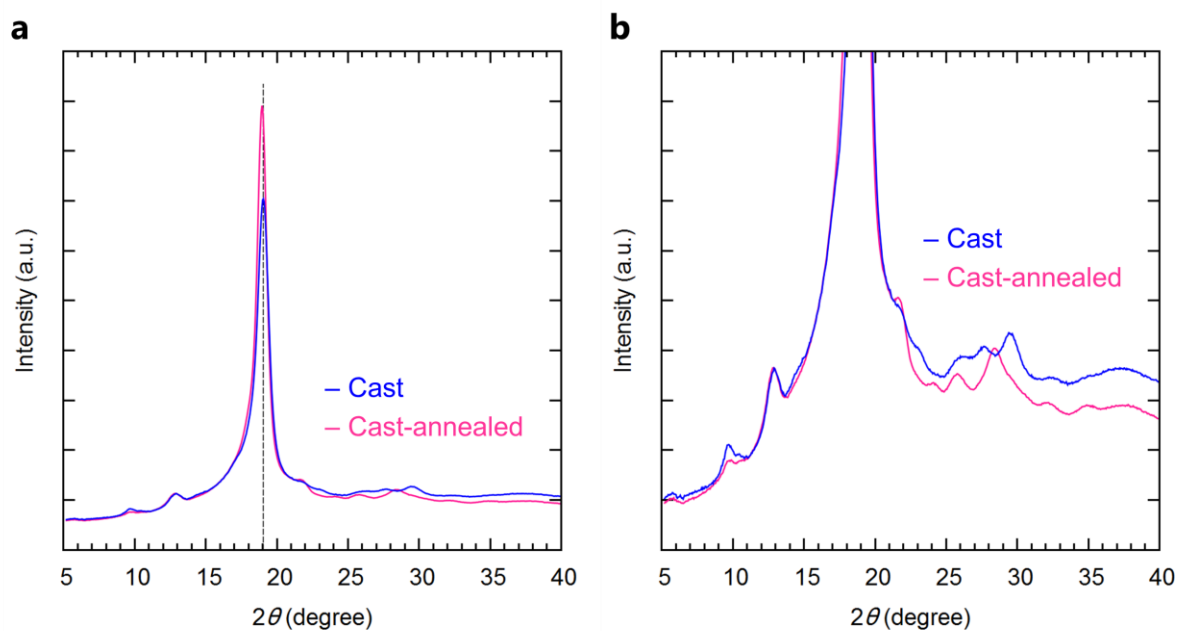


**Fig. S4.** WAXD curves of cast and cast-annealed samples: views for (a) strong and (b) weak peaks. Casting solvent is chloroform.

## S8. Fiber Diagrams of Oriented-Crystallized Films

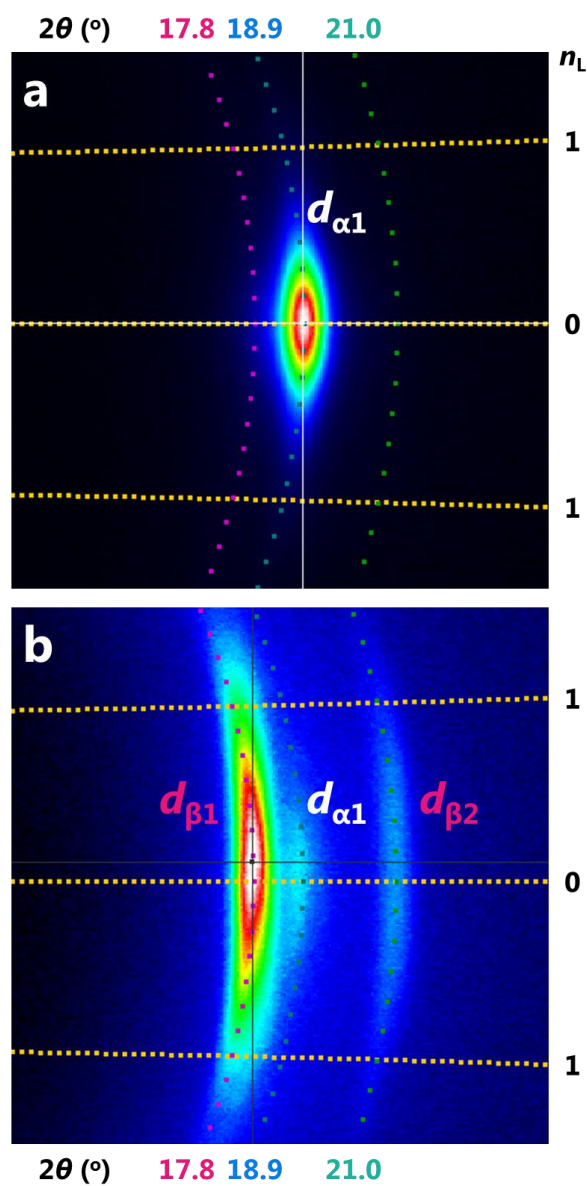


**Fig. S5.** Magnified images around equatorial peaks of  $d_{\alpha 1}$ ,  $d_{\beta 1}$ , and  $d_{\beta 2}$  in fiber diagrams of oriented films of M4h with (a)  $\alpha$ -crystals and (b)  $\beta$ -rich crystals. Drawing direction is vertical.  $2\theta$  and layer line index ( $n_L$ ) are shown for eye guide.

## S9. Peak Extraction from Fiber Diagram

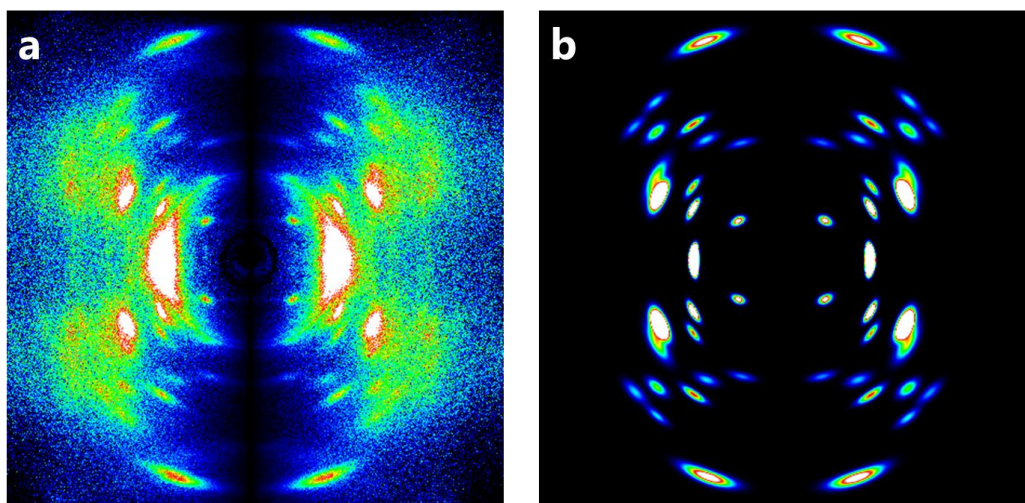


**Fig. S6.** Fiber diagrams of  $\alpha$ -form of M4h: (a) intensity-corrected pattern by eq S3 and (b) extracted peaks by peak separation using 3D Gaussian functions and quadric surface background.

## S10. Molecular Building of M4

**Table S1.** Bond lengths of M4.

Atoms & Bonds	Bond length (Å)
O(1)–C(1)	1.450
C(1)–C(2)	1.526
C(2)–O(2)	1.445
O(2)–C(3)	1.452
C(3)–C(4)	1.519
C(4)–O(3)	1.440
O(3)–C(5)	1.441
C(5)–C(6)	1.511
C(6)–O(4)	1.450
O(4)–C(7)	1.320
C(7)–C(8)	1.510
C(8)–C(9)	1.510
C(9)–C(10)	1.510
C(10)–O(1)′	1.320
C(7)–O(5)	1.190
C(10)–O(6)	1.190

**Table S2.** Bond angles of M4.

Atoms & Bonds	Bond angle (°)
O(1)–C(1)–C(2)	114.3
C(1)–C(2)–O(2)	105.1
C(2)–O(2)–C(3)	109.3
O(2)–C(3)–C(4)	106.3
C(3)–C(4)–O(3)	106.1
C(4)–O(3)–C(5)	109.4
O(3)–C(5)–C(6)	105.0
C(5)–C(6)–O(4)	114.3
C(6)–O(4)–C(7)	116.3
O(4)–C(7)–C(8)	111.0
C(7)–C(8)–C(9)	112.1
C(8)–C(9)–C(10)	112.1
C(9)–C(10)–O(1)′	111.0
C(10)–O(1)′–C(1)′	116.3
O(4)–C(7)–O(5)	123.3
C(9)–C(10)–O(6)	125.7

**Table S3.** Torsional angles of M4.

Atoms & Bonds	Abbreviation	Torsional angle (°)
O(1)–C(1)–C(2)–O(2)	-	-161.0
C(1)–C(2)–O(2)–C(3)	-	22.8
C(2)–O(2)–C(3)–C(4)	-	0.8
O(2)–C(3)–C(4)–O(3)	-	92.0
C(3)–C(4)–O(3)–C(5)	-	1.1
C(4)–O(3)–C(5)–C(6)	-	23.0
O(3)–C(5)–C(6)–O(4)	-	-161.0
C(5)–C(6)–O(4)–C(7)	$\psi$	-120.0
C(6)–O(4)–C(7)–C(8)	$\omega_1$	179.7
O(4)–C(7)–C(8)–C(9)	$\theta_1$	175.0
C(7)–C(8)–C(9)–C(10)	$\theta_2$	60.0
C(8)–C(9)–C(10)–O(1)′	$\theta_3$	170.0
C(9)–C(10)–O(1)′–C(1)′	$\omega_2$	-179.7
C(10)–O(1)′–C(1)′–C(2)′	$\varphi$	-70.0

### S11. Crystal Structure of M4 $\alpha$ -form

$$|F_c| = \sqrt{\sum m |F_{hkl}|^2} \quad (S4)$$

$$F_{hkl} = \sum_j f_j T_j \exp[2\pi i(hx_j + ky_j + lz_j)] \quad (S5)$$

$$T_j = \exp(-B_j \sin^2 \theta / \lambda^2) \quad (S6)$$

where  $F_c$  is the calculated structure factor,  $m$  is the multiplicity of the reflection,  $F_{hkl}$  is the structure factor of the  $(hkl)$  plane,  $j$  is the index of the constituent atom,  $f_j$  is the atomic scattering factor,  $(x_j, y_j, z_j)$  is the fractional coordinate in the unit cell,  $T_j$  is the Debye–Waller factor,  $B_j$  is the isotropic atomic displacement parameter ( $0.12 \text{ nm}^2$ ),  $\theta$  is the Bragg angle, and  $\lambda$  is the wavelength of X-ray ( $0.15418 \text{ nm}$ ).

**Table S4.** Observed and calculated lattice spacings ( $d_o$ ,  $d_c$ ) and structure factors ( $|F_o|$ ,  $|F_c|$ ) of M4  $\alpha$ -form. Scaling factor  $K = 0.0261$ .

No.	$h$	$k$	$l$	$d_o$ (nm)	$d_c$ (nm)	$ F_o $	$ F_c $
1	0	2	0	0.467	0.456	277	270
	1	1	0		0.454		
2	0	1	2	0.687	0.686	42	49
3	0	2	2	0.406	0.418	62	79
	1	1	2		0.416		
4	0	2	3	0.367	0.381	40	44
	1	1	3		0.380		
5	1	2	3	0.313	0.308	113	63
6	1	2	4	0.294	0.287	70	90
7	0	1	6	0.346	0.324	29	25
8	1	0	6	0.307	0.289	35	25
9	0	2	6	0.277	0.276	52	68
	1	1	6		0.276		
10	1	2	6	0.256	0.244	47	69
11	0	3	6	0.238	0.229	34	16
12	1	2	7	0.235	0.225	35	35
13	0	2	8	0.215	0.226	100	95
	1	1	8		0.226		
	0	2	9		0.206		
	1	1	9		0.206		

**Table S5.** Atomic fractional coordinates of M4  $\alpha$ -form.

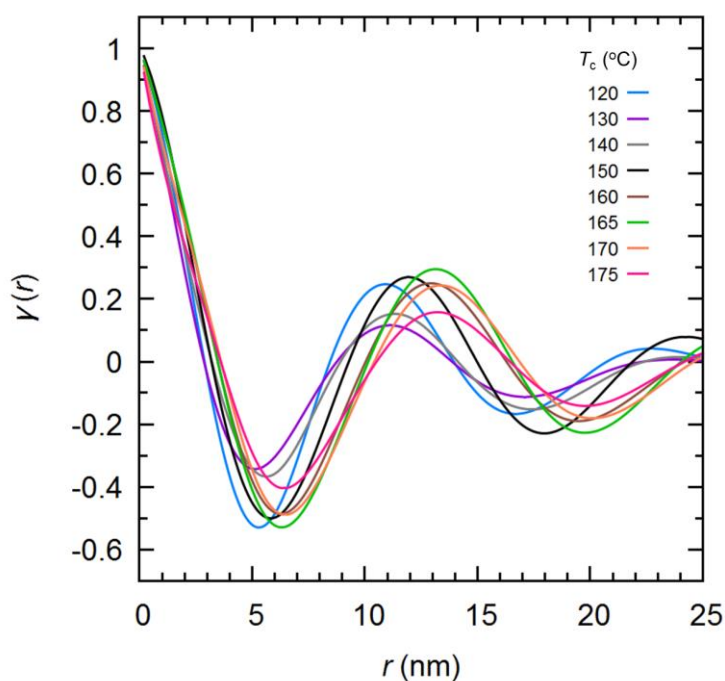
Chain	Residue	Atom	$X_f$	$Y_f$	$Z_f$
Parallel	1	O(1)	0.339	-0.084	0.122
		C(1)	0.144	-0.131	0.167
		C(2)	-0.089	-0.031	0.171
		O(2)	-0.211	-0.066	0.231
		C(3)	-0.025	-0.131	0.274
		C(4)	0.227	-0.134	0.238
		O(3)	0.356	0.000	0.254
		C(5)	0.202	0.083	0.298
		C(6)	0.031	-0.029	0.330
		O(4)	-0.193	0.033	0.361
	C(7)	-0.216	0.009	0.423	
	C(8)	-0.456	0.080	0.449	
	C(9)	-0.498	0.044	0.519	
	C(10)	-0.280	0.096	0.561	
	O(5)	-0.064	-0.058	0.454	
	O(6)	-0.081	0.141	0.542	
	2	O(1)	-0.339	0.084	0.622
		C(1)	-0.145	0.132	0.667
		C(2)	0.089	0.032	0.671
		O(2)	0.211	0.067	0.731
C(3)		0.024	0.132	0.774	
C(4)		-0.227	0.134	0.738	
O(3)		-0.356	-0.001	0.754	
C(5)		-0.202	-0.083	0.798	
C(6)		-0.031	0.029	0.830	
O(4)		0.194	-0.032	0.861	
C(7)	0.216	-0.009	0.923		
C(8)	0.456	-0.079	0.949		
C(9)	0.498	-0.043	1.019		
C(10)	0.281	-0.096	1.061		
O(5)	0.064	0.058	0.954		
O(6)	0.081	-0.141	1.042		
Parallel	1	O(1)	0.868	0.520	0.000
		C(1)	0.737	0.425	0.045
		C(2)	0.449	0.448	0.048
		O(2)	0.371	0.384	0.109
		C(3)	0.589	0.378	0.152
		C(4)	0.812	0.446	0.115
		O(3)	0.812	0.599	0.132
		C(5)	0.607	0.629	0.176
		C(6)	0.552	0.483	0.208
		O(4)	0.303	0.475	0.238
	C(7)	0.303	0.448	0.301	
	C(8)	0.034	0.443	0.327	
	C(9)	0.027	0.400	0.397	
	C(10)	0.174	0.506	0.439	
	O(5)	0.493	0.431	0.331	
	O(6)	0.310	0.601	0.420	
	2	O(1)	0.132	0.480	0.500
		C(1)	0.262	0.575	0.545
		C(2)	0.551	0.553	0.548
		O(2)	0.628	0.617	0.609
C(3)		0.410	0.622	0.652	
C(4)		0.188	0.554	0.616	
O(3)		0.189	0.401	0.631	
C(5)		0.394	0.371	0.676	
C(6)		0.448	0.517	0.708	
O(4)		0.697	0.526	0.738	
C(7)	0.697	0.552	0.801		
C(8)	0.966	0.558	0.827		
C(9)	0.972	0.601	0.897		
C(10)	0.826	0.494	0.939		
O(5)	0.506	0.569	0.831		
O(6)	0.691	0.399	0.920		

## S12. Correlation Function Analysis of SAXS Data

Each SAXS curve [ $I(q)$  vs  $q$ , where  $I(q)$  is the scattering intensity and  $q$  is the scattering vector ( $q = 4\pi\sin\theta/\lambda$ )] was converted to the normalized one-dimensional correlation function [ $\gamma(r)$ ]:<sup>S1</sup>

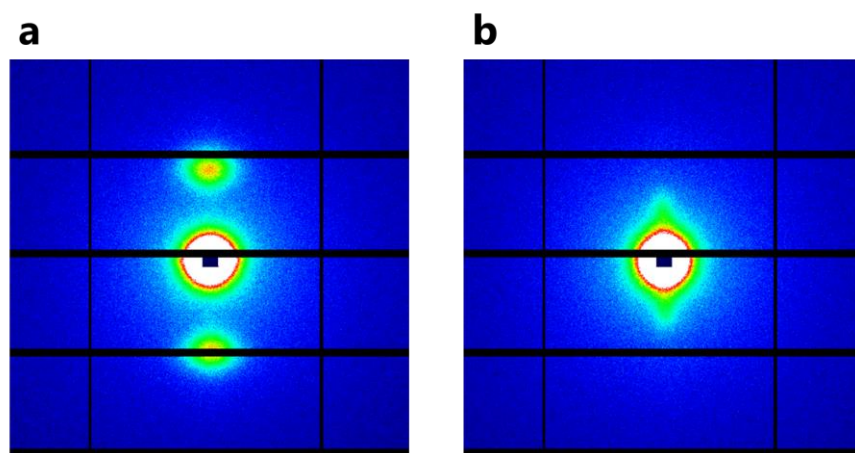
$$\gamma(r) = \frac{\int_0^\infty q^2 I(q) \cos(qr) dq}{\int_0^\infty q^2 I(q) dq} \quad (S7)$$

where  $r$  is the correlation length (nm). Integral calculations were executed for  $0 \leq q \leq q_{\text{cutoff}}$ , where  $q_{\text{cutoff}}$  is the scattering vector at which the calculated value of  $q^2 I(q)$  becomes a sufficiently small value.  $I(q)$  in a relatively low  $q$  range ( $0 \leq q \leq 0.2\text{--}0.3 \text{ nm}^{-1}$ ) was calculated according to the Guinier law<sup>S2</sup> and  $I(q)$  in a relatively high  $q$  range ( $q > 1.1\text{--}1.7 \text{ nm}^{-1}$ ) was determined on the basis of the Porod law.<sup>S2</sup> Based on the lamellar two-phase model, the long period ( $L_p$ ), lamella thickness ( $l_c$ ), and amorphous layer thickness ( $l_a$ ) were determined from  $\gamma(r)$  by the method of Strobl and Schneider.<sup>S3</sup> The value of  $-w/(100 - w)$ , where  $w = X_c$  for  $X_c < 50\%$  and  $w = 100 - X_c$  for  $X_c \geq 50\%$ , was used as a baseline determining the lamella and amorphous layer thicknesses, respectively, although volume crystallinity should be used to be exact.<sup>S4</sup>

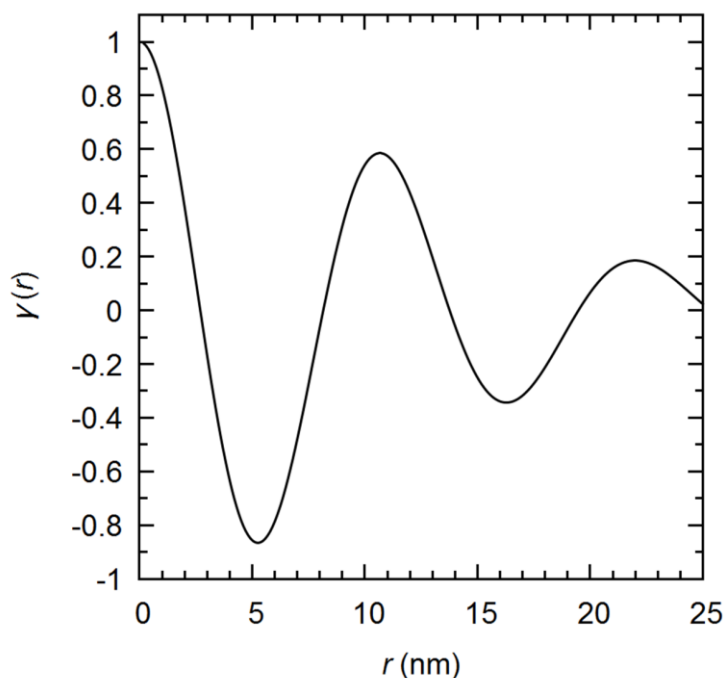


**Fig. S7.** Normalized one-dimensional correlation functions [ $\gamma(r)$ ] of M4 melt-crystallized at various temperatures.

### S13. 2D SAXS of Oriented-Crystallized Films

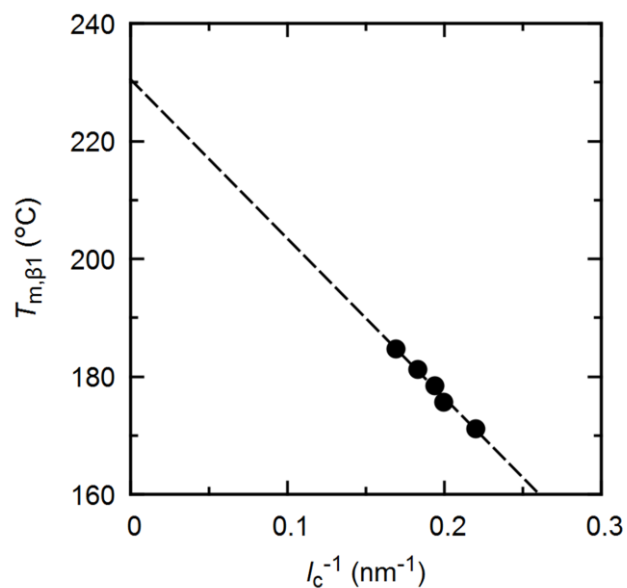


**Fig. S8.** 2D SAXS patterns of oriented-crystallized films of M4h with (a) pure  $\alpha$ -crystals; (b)  $\beta$ -crystals and a small number of  $\alpha$ -crystals. Drawing direction is vertical. SAXS measurements were conducted by using synchrotron X-ray ( $\lambda = 0.1488$  nm) at room temperature.

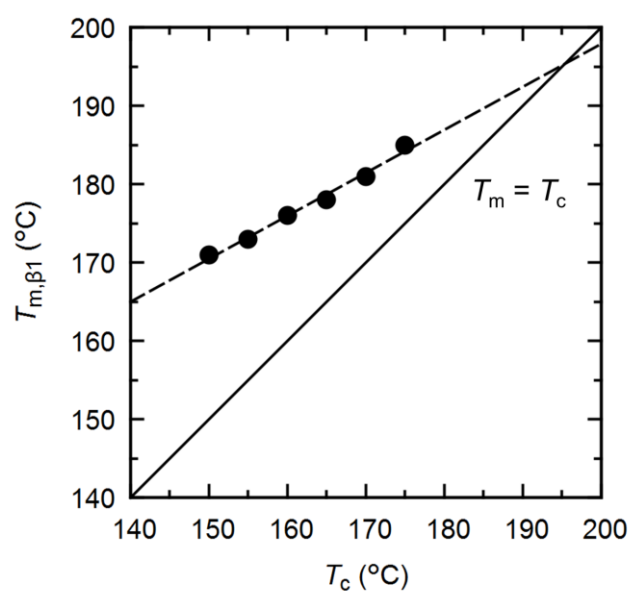


**Fig. S9.** Normalized one-dimensional correlation function [ $\gamma(r)$ ] of oriented-crystallized film of M4h with pure  $\alpha$ -crystals. Correlation function analysis was performed for the azimuthally-averaged profile around the peak in 2D SAXS pattern.

#### S14. Estimation of Equilibrium Melting Temperature ( $T_m^\circ$ )



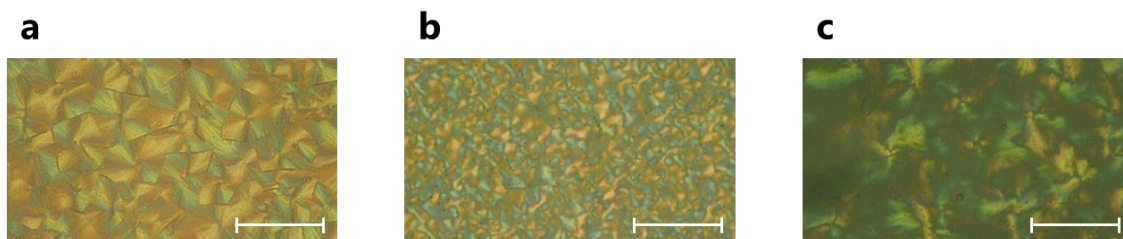
**Fig. S10.**  $T_{m,\beta 1}$  of M4 crystallized at  $T_c \geq 150$  °C plotted against  $l_c^{-1}$  with the regression line, whose intercept yields  $T_m^\circ$  of the  $\beta$ -form (Gibbs–Thomson plot).



**Fig. S11.**  $T_{m,\beta 1}$  vs  $T_c$  plots for M4 crystallized at  $T_c \geq 150$  °C with the regression line, whose intersection with the line  $T_m = T_c$  yields  $T_m^\circ$  of the  $\beta$ -form (Hoffman–Weeks plot).

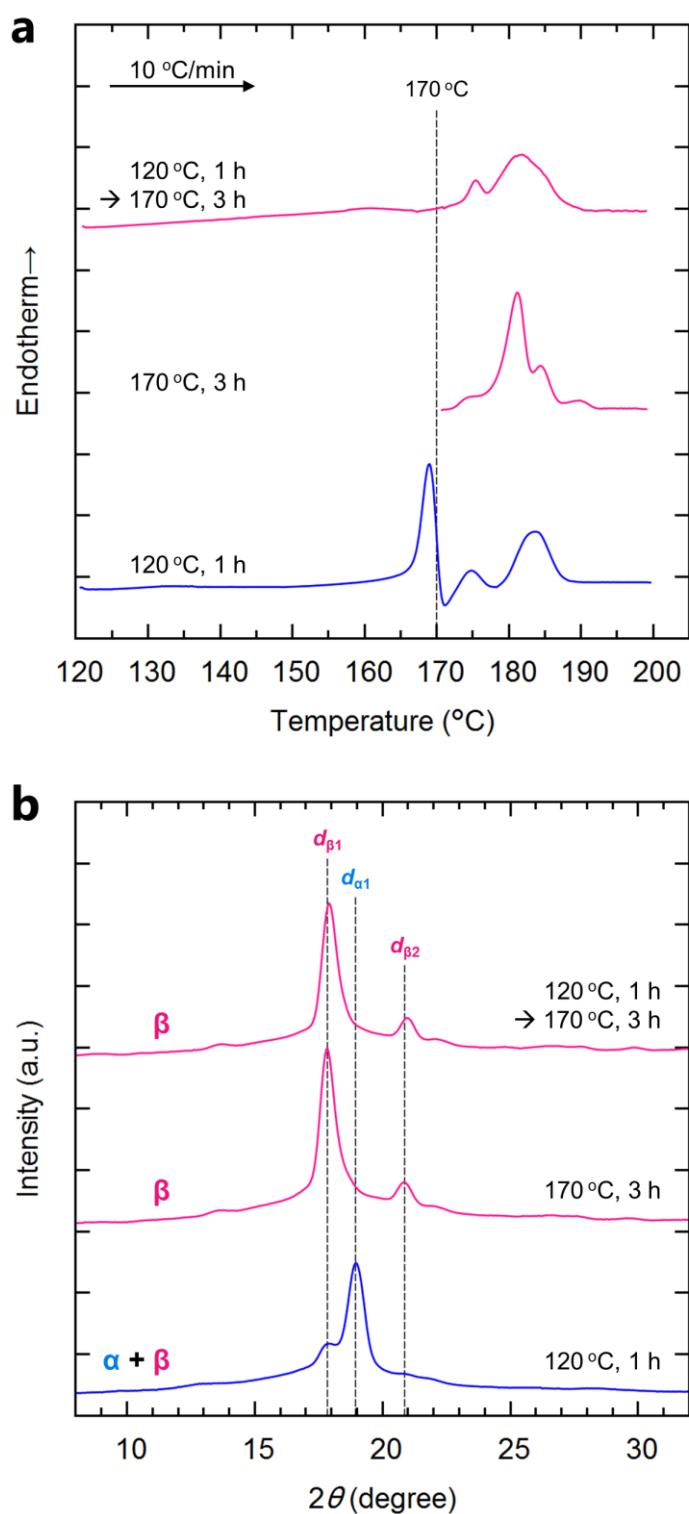
### S15. Crystalline Morphology

Fig. S12 shows POM images of M4 melt-crystallized at  $T_c = 120, 140,$  and  $160\text{ }^\circ\text{C}$ . Negatively birefringent spherulites are seen at  $T_c = 120\text{ }^\circ\text{C}$ . Interestingly, disordered spherulites whose size is smaller than that of spherulites at  $T_c = 120\text{ }^\circ\text{C}$ , are observed at  $T_c = 140\text{ }^\circ\text{C}$ . Such an unusual morphological change should be linked with the crystal polymorphism of  $\alpha$ - and  $\beta$ -forms, because in general the spherulite size increases with increasing  $T_c$  (i.e., decreasing the degree of supercooling) owing to a decrease in the nucleation density.<sup>S5</sup> As mentioned in the section 3.1.1 (Figure 2), a mixture of  $\alpha$ - and  $\beta$ -forms whose fractions are comparable is generated at  $T_c = 140\text{ }^\circ\text{C}$ , so that the  $\alpha$ -form crystals might act as nucleating agents for the  $\beta$ -form crystals and vice versa. Sheaf-like crystals rather than spherulites are seen at  $T_c = 160\text{ }^\circ\text{C}$ . The size of sheaf-like crystals at  $T_c = 160\text{ }^\circ\text{C}$  is comparable or slightly larger than that of spherulites at  $T_c = 120\text{ }^\circ\text{C}$ .



**Fig. S12.** POM images of M4 melt-crystallized at  $T_c =$  (a) 120, (b) 140, or (c) 160  $^\circ\text{C}$ . Each scale bar represents 50  $\mu\text{m}$ .

### S16. Effect of Re-annealing on Crystal Structure of Melt-crystallized M4 ( $\alpha$ -rich)



**Fig. S13.** (a) DSC heating curves and (b) WAXD profiles of M4 melt-crystallized in different conditions to show the effect of re-annealing at  $170\text{ }^{\circ}\text{C}$ .

## References

- (S1) Vonk, C. G.; Kortleve, G. X-ray Small-Angle Scattering of Bulk Polyethylene. II. Analyses of the Scattering Curve. *Colloid Polym. Sci.* **1967**, *220*, 19–24.
- (S2) (a) Roe, R.-J. *Methods of X-ray and Neutron Scattering in Polymer Science*; Oxford University Press: New York, 2000. (b) Stribeck, N. *X-Ray Scattering of Soft Matter*; Springer-Verlag: Berlin, 2007.
- (S3) Strobl, G. R.; Schneider, M. Direct Evaluation of the Electron Density Correlation Function of Partially Crystalline Polymers. *J. Polym. Sci., Polym. Phys. Ed.* **1980**, *18*, 1343–1359.
- (S4) Baltá-Calleja, F. J.; Vonk, C. G. *X-ray scattering of synthetic polymers*; Elsevier: Amsterdam, 1989; pp 241–306.
- (S5) Marubayashi, H.; Nojima, S. Crystallization and Solid-State Structure of Poly(L-2-hydroxy-3-methylbutanoic acid). *Macromolecules* **2016**, *49*, 5538–5547.